Geochemistry Geophysics Geosystems G3

Article
Volume 11, Number 12
15 December 2010
Q12008, doi:10.1029/2010GC003270
ISSN: 1525-2027

Published by AGU and the Geochemical Society

Generation of permeability barriers during melt extraction at mid-ocean ridges

Laura B. Hebert and Laurent G. J. Montési

Department of Geology, University of Maryland, College Park, Maryland 20742, USA (lhebert@geol.umd.edu)

[1] Melt focusing at mid-ocean ridges is necessary to explain the narrowness of the zone of crustal accretion and the formation of large but localized on-axis seamounts at slow and ultraslow spreading centers. It has been proposed that melt focusing is facilitated by the presence of a barrier to upward melt migration at the base of the thermal boundary layer (TBL). We assess the development of a melt impermeable boundary by modeling the geochemical evolution and crystallization history of melts as they rise into the TBL of mid-ocean ridges with different spreading rates. A permeability barrier, associated with a crystallization front controlled by the conductive thermal regime, exists for melt trajectories at slow to fast spreading ridges (≥10 mm/yr half rate). The effective lateral scope of the barrier, where the slope of the barrier exceeds a critical value that allows buoyant melt transport to the axis, generally increases with spreading rate. At all distances from the axis at ultraslow ridges and off-axis at slow spreading ridges, the weak crystallization front may prohibit formation of an efficient barrier and lead to the possibility that some fraction of melt may be incorporated into the lithospheric mantle, allowing refertilization. The protracted crystallization history and potential absence of an effective permeability barrier may explain the dearth of volcanism at ultraslow ridges and calls for a revision of lateral melt focusing scenarios at ultraslow spreading rates.

Components: 11,300 words, 7 figures.

Keywords: permeability barrier; lithosphere; mantle melting; mid-ocean ridge.

Index Terms: 3610 Mineralogy and Petrology: Geochemical modeling (1009, 8410); 3614 Mineralogy and Petrology: Mid-oceanic ridge processes (1032, 8416); 0599 Computational Geophysics: General or miscellaneous.

Received 23 June 2010; **Revised** 24 September 2010; **Accepted** 4 November 2010; **Published** 15 December 2010.

Hebert, L. B., and L. G. J. Montési (2010), Generation of permeability barriers during melt extraction at mid-ocean ridges, *Geochem. Geophys. Geosyst.*, *11*, Q12008, doi:10.1029/2010GC003270.

1. Introduction

[2] The focusing of melt beneath mid-ocean ridges (MORs) from a broad (potentially several hundred kilometers wide) partially molten zone at depth [*The MELT Seismic Team*, 1998] into a narrow (1–2 km wide) neovolcanic zone at the axis [e.g., *Macdonald*, 1982; *Sinton and Detrick*, 1992] remains a challenging observation for geodynamics to explain. Variations in crustal thickness may reflect focusing systematics controlled by geometrical effects and/or the thermal structure of the mantle near the axis. For example, along-axis melt focusing is likely the source of crustal thickness heterogeneities related to ridge segmentation [*Hooft et al.*, 2000; *Cannat et al.*, 1995; *Dunn et al.*, 2005; *Gregg et al.*, 2009; *Planert et al.*, 2009]. Spreading rate, which largely controls the thermal structure beneath MORs, generally correlates positively with crustal thickness, whether inferred from axial depth, geochemical modeling, or seismic observations [*Klein and Langmuir*, 1987; *White et al.*, 2001; *Niu and*

Copyright 2010 by the American Geophysical Union

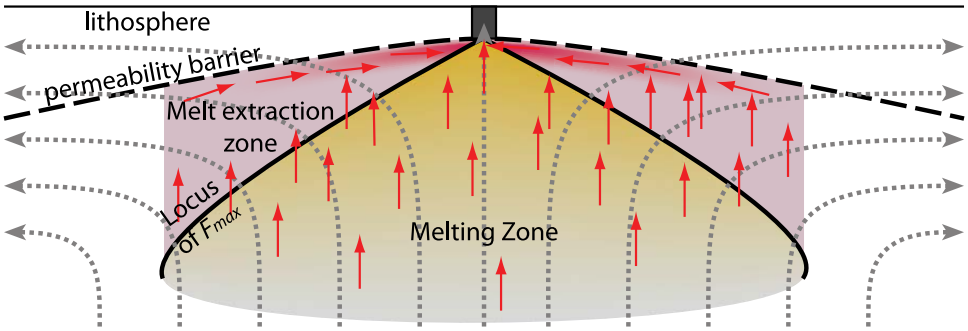

Figure 1. Cartoon illustrating the melt focusing scenario studied in this contribution. Melts are produced in the active melting zone (yellow shading) and rise buoyantly (red arrows) to the thermal boundary layer (TBL) at the base of the lithosphere where they crystallize and may form a permeability barrier (thick dashed line). Melts will then migrate along this boundary, following the sloping basal topography until they reach the neovolcanic zone (black box) and erupt. Solid flow streamlines are denoted by gray dotted arrows, and the thick solid line indicates the depth where the equilibrium fraction is maximum (F_{max}). The pink shading represents melt porosity in the melt extraction zone, where active melting is no longer occurring. Melt accumulates in a decompaction channel immediately below the permeability barrier.

O'Hara, 2008]. However, there is a wider variation in crustal thickness measurements for slower spreading ridges as compared with faster spreading ridges [*Chen*, 1992], perhaps suggesting a changing means of melt delivery toward the axis as a function of spreading rate. Ultraslow spreading ridges (less than ~10 mm/yr half rate) are characterized by discontinuous magmatism at localized volcanic centers separated by amagmatic segments [*Michael et al.*, 2003; *Dick et al.*, 2003] indicating a more complex focusing mechanism through a thick thermal boundary.

[3] Proposed mechanisms for focused ridge magmatism include (1) large pressure gradients that focus the flow of melt [*Phipps Morgan*, 1987; *Spiegelman and McKenzie*, 1987; *Ribe*, 1988], (2) buoyancy-driven convection due to lateral variations in melt content [*Rabinowicz et al.*, 1984; *Buck and Su*, 1989; *Scott and Stevenson*, 1989], (3) hydrofracturing [*Sleep*, 1988; *Nicolas*, 1990], (4) development of a stress-induced anisotropic permeability [*Phipps Morgan*, 1987; *Katz et al.*, 2006], (5) reaction-infiltration instability [*Aharonov et al.*, 1995; *Kelemen and Dick*, 1995; *Kelemen et al.*, 1995a, 1995b], leading to (6) a fractal melt extraction tree [*Hart*, 1993] and (7) development of a high-porosity channel along the base of the sloping lithosphere, allowing melt to flow toward the ridge axis (Figure 1) [*Sparks and Parmentier*, 1991; *Spiegelman*, 1993a, 1993b; *Ghods and Arkani-Hamed*, 2000; *Katz*, 2008]. Mechanisms 1 and 2 are unlikely to play an important role as they require higher viscosities or lower porosities than currently estimated beneath MOR spreading centers and mechanisms 3–6 remain to be fully tested. Here, we focus on evaluating the potential role of mechanism 7 in melt focusing at MORs.

[4] Mechanism 7 is based on the interaction of a melt propagating as a pore fluid within a solid viscous matrix and through the thermal boundary layer (TBL) present at the base of lithospheric plates. Crystallization-driven decompaction of the porous matrix beneath the barrier forms a high-porosity channel [*Ribe*, 1985; *Spiegelman*, 1993c], the thickness of which is determined by the balance between melt buoyancy and viscous stresses [*Sparks and Parmentier*, 1991]. The channel follows the base of the TBL, which is shallower underneath the ridge axis. Therefore, buoyant magma may follow the channel and can be focused toward the axis. Channel formation occurs near where vertically propagating melt begins crystallizing within the TBL [*Sparks and Parmentier*, 1991]. *Spiegelman* [1993c] and *Rabinowicz and Ceuleneer* [2005] demonstrated that solitary waves generated at the freezing boundary facilitate the formation of high-porosity channels. The greater the freezing rate or, equivalently, the narrower the freezing region, the more likely a melt channel will form [*Spiegelman*, 1993c]. In other words, the efficiency of focusing depends on the ratio of the length scale of the crystallization region to the local compaction length, and an effectively open channel will develop if the crystallizing region is restricted compared to the compaction length [*Spiegelman*, 1993c]. The melt impermeable freezing boundary, or permeability barrier, thus has an integral connection to the crystallization behavior

of upwelling melts both immediately beneath and at increasing distances away from the axis of the spreading center. In this contribution, we utilize petrological modeling to describe crystallization patterns and predict the location and efficiency of a 2-D melt permeability barrier at MORs of diverse spreading rate.

[5] The permeability barrier model of melt focusing at mid-ocean ridges has been used to explain along strike variations in crustal thickness as well as erupted basaltic compositions for spreading centers of varying divergence rates. Melt transport along a permeability barrier has been proposed to explain lava chemistry at the ultraslow Southwest Indian Ridge (SWIR) between 9°E and 25°E [*Standish et al.*, 2008]. Deeply originating, low-degree melts seem to be redistributed from beneath the thick lithosphere along amagmatic segments toward neighboring magmatic segments with thinner lithosphere, explaining the unusual enrichment in K_2O and the high K/Ti of basalts recovered from the area [*Standish et al.*, 2008]. Based on analysis of transform and ridge segment length along the Mid-Atlantic Ridge at 33°N–35°N, a permeability barrier has been found to be more efficient than diapiric instabilities for focusing magma at slow spreading rates (15 mm/yr half rate) [*Magde and Sparks*, 1997; *Magde et al.*, 1997]. *Gregg et al.* [2009] proposed that focusing along the base of the lithosphere might explain the magmatic activity of Intra-Transform Spreading Centers at the Siqueiros transform of the ultrafast East Pacific Rise. Lateral melt transport within a channel beneath a melt impermeable boundary may be rapid, explaining observed excesses of ^{226}Ra and ^{230}Th [*Sims et al.*, 2002; *Jull et al.*, 2002] in lavas at ultraslow spreading centers [*Standish and Sims*, 2010].

[6] The impermeable freezing boundary has been described in structural and petrological terms on the basis of observations from the Oman ophiolite [*Ceuleneer and Rabinowicz*, 1992; *Korenaga and Kelemen*, 1997; *Kelemen and Aharonov*, 1998]. A transition from continuous porous flow to punctuated formation of melt-filled fractures is inferred at the position of layered gabbroic sills [*Kelemen and Aharonov*, 1998]. Repeated injection of sills is consistent with melt accumulating in a decompaction layer at the base of a permeability barrier. Seismic reflection studies beneath the southern Juan de Fuca ridge (56 mm/yr half rate [e.g., *Wilson*, 1993]) have imaged molten sills within the lower crust [*Canales et al.*, 2009] and within a thick subcrustal zone up to 30 km off axis [*Nedimović et al.*, 2005]. Compliance measurements used to estimate melt distribution beneath the fast spreading East Pacific Rise showed several off-axis (~10–14 km) melt zones present at lower crustal depths [*Crawford and Webb*, 2002]. These studies provide evidence for the possible existence of channelized melt transport beneath permeability barriers within intermediate to fast spreading ridge systems.

[7] The position of a permeability barrier is likely controlled by the crystallization sequence of melts as they percolate vertically and encounter the TBL beneath the ridge, where conductive cooling becomes significant. Crystallization of multiply saturated basaltic liquids within a porous medium will result in a strong reduction in porosity and permeability [*Kelemen and Aharonov*, 1998]. Thus, in terms of crystallizing species, a permeability barrier would most likely be associated with the saturation of plagioclase ± clinopyroxene as a consequence of the rapid drop in liquid mass with continued cooling associated with the onset of crystallization of these minerals [*Korenaga and Kelemen*, 1997; *Kelemen and Aharonov*, 1998]. The Moho transition zone (MTZ) characterized by the presence of layered gabbroic sills [*Ceuleneer and Rabinowicz*, 1992; *Rabinowicz and Ceuleneer*, 2005] is associated by *Kelemen and Aharonov* [1998] with the transition from vertically upwelling porous flow at the level of plagioclase (±clinopyroxene) saturation in ascending magmas. *Kelemen and Aharonov* [1998] modeled crystallization by decreasing temperature at constant pressure representing the base of the crust, as may be appropriate immediately underneath the axis of fast spreading centers. Here, we will consider the progressive depressurization of magma coincident with cooling, which captures more realistically the evolution of a rising melt entering the TBL off axis at faster spreading centers and at slower spreading rates.

[8] The thickness of the TBL, and therefore the location of the permeability barrier, should vary as a function of spreading rate. With decreasing spreading rate, the increasing influence of conductive cooling results in a thicker TBL and, by restricting the top of the melting region, reduced melt volume [*Reid and Jackson*, 1981; *Bown and White*, 1994; *Shen and Forsyth*, 1995; *Niu and Hékinian*, 1997; *Dick et al.*, 2003]. The position of the MTZ is also expected to vary with spreading rate: it may be present over a wide depth interval at slow ridges [e.g., *Cannat*, 1996], whereas at fast to medium spreading ridges, the MTZ may be present only at a narrow depth interval immediately below the crust [*Kelemen and Aharonov*, 1998]. Positions of potential permeability barriers are typically

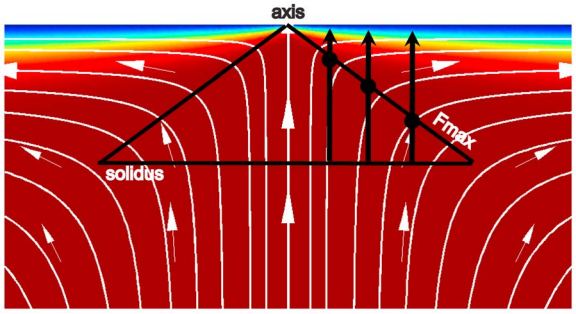

Figure 2. Example of the mantle flow and thermal structure model used in this study. The colors indicate temperature, from 0°C (blue) to 1375°C (red). Streamlines representing the analytical solution for the flow field are shown as thin, white lines. A schematic triangular melting region is shown within the thin, black lines. The base of the melting region is shown as the position of the solidus. The top of the triangular melting region is denoted by the location of F_{max}, where the maximum degree of melting of upwelling mantle material is reached. Calculation columns are defined at increasing distance from the axis.

associated with the top of the melting column [*Sparks and Parmentier*, 1991; *Magde et al.*, 1997] or to a crystallization function directly related to the melting relation [*Ghods and Arkani-Hamed*, 2000; *Katz*, 2008]. *Montési and Behn* [2007] developed a simple prediction of the depth of a permeability barrier:

$$T_{barrier} = 1240^{\circ}\mathrm{C} + 1.9z, \tag{1}$$

where $T_{barrier}$ is temperature of the permeability barrier in °C, and z is depth in kilometers. This relation is based on the correlation of a permeability barrier with the temperature of the plagioclase multiple saturation point [*Kelemen and Aharonov*, 1998], proposed to increase with depth at a rate of 58°C/GPa [*Yang et al.*, 1996]. In this work, we will further refine the predicted depth of permeability barrier using a full thermodynamical formulation.

[9] Many studies of melting at MOR have used 1-D "column" modeling [*Ribe*, 1985; *Asimow and Stolper*, 1999; *Hewitt and Fowler*, 2008]. The present work considers melting and crystallization columns at various distances from the axis of ridges with various spreading rates. We model the evolution of magma batches as they rise through the TBL of MORs and determine at what depth crystallization rate is maximum as a proxy to a potential permeability barrier. We also evaluate the strength of the proposed barrier. This model implies that focusing along a permeability barrier is efficient at most spreading rates but that different focusing mechanisms, or a different origin of the permeability barrier, may be necessary for ultraslow spreading centers.

2. Methods

[10] Our model of formation of a permeability barrier is computed in three steps. First, we model the thermal structure underneath a spreading center for a given spreading rate. Then, we use a melting model to compute the composition of melt formed by decompression melting in each on- or off-axis 1-D column. Finally, we simulate crystallization of the aggregate melt in the TBL and determine at what depth a permeability barrier is most likely to form. The model is repeated for different off-axis distances and for different spreading rates.

2.1. Mid-ocean Ridge Thermal and Flow Solution

[11] The temperature structure underneath the ridge (Figure 2) is modeled using the Finite Element software package COMSOL Multiphysics® 3.4. We impose velocity given by the analytical 2-D corner flow solution for the flow potential ϕ underneath a passive spreading center [e.g., *Batchelor*, 1967; *McKenzie*, 1969]:

$$\phi = \frac{2}{\pi} U_0 r\theta \cos\theta \tag{2}$$

$$\begin{cases} u_x = -\partial\phi/\partial z \\ u_z = \partial\phi/\partial x \end{cases}, \tag{3}$$

The solution is expressed in cylindrical coordinates aligned with the ridge axis where r is the radial distance from the ridge, θ is the angle from the vertical, and horizontal half-rate U_0 ranges from ultraslow to fast spreading velocities (U_0 = <10 to 100 mm/yr). This solution assumes that the flow is solely driven by the divergence of rigid plates at the surface and it ignores the contribution of buoyancy. While this assumption is more appropriate for fast spreading centers, *Magde et al.* [1997] demonstrated that buoyant upwellings exert a lesser control on crustal thickness variations than focusing along a permeability barrier. Even at ultraslow spreading centers, it is possible to reproduce crustal thickness variations while ignoring the contribution of buoyancy to mantle upwelling (L. G. J. Montési et al., Crustal variations at the Southwest Indian

Ridge 10°E–16°E oblique supersegment: The plate-driven view, manuscript in preparation, 2010).

[12] We solve the following formulation for thermal convection and conduction:

$$\nabla \cdot (-\kappa \nabla T) = -(\mathbf{u} \cdot \nabla T), \quad (4)$$

where **u** is mantle velocity defined above, T is temperature, and $\kappa = 10^{-6}$ m^2/s is the thermal diffusivity. A mantle potential temperature (T_P = 1375°C) sets the bottom of the model space and the top surface of the model space is set to T_S = 0°C. The side boundaries are open to convective flux, implying that there is no diffusive heat transfer across these boundaries. The Finite Element grid spacing, using triangular elements, decreases toward the surface and toward the ridge axis in order to resolve the thermal structure for spreading rates considered in this study. An adiabatic temperature gradient (0.7°C/km) is imposed on the model result after steady state has been achieved.

2.2. Melt Migration and Crystallization

[13] We use the thermodynamics software MELTS [*Ghiorso and Sack*, 1995; *Asimow and Ghiorso*, 1998] in conjunction with the Adiabat_1ph user interface [*Smith and Asimow*, 2005] to solve for melt compositions and for fractional crystallization. We selected an anhydrous starting composition (DMM [*Workman and Hart*, 2005]). Our calculations follow a two-step chemical evolution using the pressure and temperature conditions in a series of one-dimensional, vertical columns extracted from the flow model and temperature solution (Figure 2). We assume that melt travels vertically under a buoyancy-dominated regime. We consider a series of columns at different distances away from the spreading axis, in order to capture the potentially different crystallization behaviors and compositions of melts generated from different regions of the quasi-triangular melting region.

[14] We first perform an equilibrium melting calculation within each column, beginning at a pressure of 2 GPa (~62 km depth) and continuing vertically until the maximum melt fraction (F_{max}) is encountered. This encompasses the active partial melting regime beneath the spreading center, defined by an initial pressure of melting P_0 and different values for final pressure of melting P_F, depending on the distance from the axis. At the depth of F_{max} (P_F for each column), roughly coincident with the location of solid streamline turnover in corner flow (Figures 1 and 2), we assume that the melt continues to travel vertically. Even though solid flow lines are subhorizontal, melt continues to migrate vertically because permeability is high enough for melt velocities to exceed solid mantle velocities [*McKenzie*, 1985; *Spiegelman and Elliott*, 1993; *Lundstrom et al.*, 1995; *Sims et al.*, 2002] and buoyancy contrast dominates over flow in inducing pressure gradients for reasonable mantle viscosities [*Spiegelman and McKenzie*, 1987; *Phipps Morgan*, 1987]. Dissolution instabilities further facilitate vertical melt extraction [*Kelemen and Dick*, 1995], but we do not consider the chemical effects of forming a channelized melt extraction network.

[15] The melts produced deeper than F_{max} are aggregated to produce the starting melt composition for the second step of our thermodynamics model. We perform a batch crystallization calculation to find the change in mass and composition of this aggregate melt under decreasing temperature and pressure conditions as the melt rises into the TBL. In addition to tracking the rate of crystallization, we monitor the partial crystallization process in terms of the identity and sequence of mineral-in reactions. The thermal model is sampled every 25 m, resulting in pressure steps to MELTS of approximately 8 bars. The fine sampling interval is necessary to capture the first appearance of phases in order to accurately assess the crystallization behavior, especially within the very thin TBL associated with the faster spreading cases.

[16] We do not address the effects of a changing starting composition on our results in this study. This may be significant especially with regard to water (H_2O) and sodium (Na_2O). Increasing H_2O and Na_2O in the mantle source composition both allow for an increased pressure of initial melting [*Klein and Langmuir*, 1987; *Asimow and Langmuir*, 2003]. Addition of H_2O to the MOR basalt source may suppress plagioclase crystallization relative to olivine and clinopyroxene [*Yoder*, 1965; *Gaetani et al.*, 1993; *Sisson and Grove*, 1993]. We also neglect wall rock reaction. While MELTS provides a self-consistent thermodynamic approach, and the Adiabat_1ph interface allows for rapid calculations necessary to sample the large model space, limitations of the program must be acknowledged. Experimental comparison demonstrates that MELTS overestimates the incompatibility of sodium in the spinel peridotite field [*Hirschmann et al.*, 1998]. Additionally, there are systematic offsets in temperature and in the concentrations of oxides such as SiO_2 and MgO when compared to experiments [*Baker et al.*, 1995]. However, even with these shortcomings, MELTS is a widely used and

sophisticated tool that allows an integrated and self-consistent treatment of peridotite partial melting.

2.3. Time Scales of Deformation and Crystallization

[17] *McKenzie* [1984] demonstrated that fluids migrating in a viscous porous matrix can develop pressure gradients over length scales limited by the compaction length:

$$\delta_c = \sqrt{\frac{k_\theta\left(\xi + \frac{4}{3}\eta\right)}{\mu}}, \tag{5}$$

where k_θ is permeability, ξ and η are bulk and shear viscosities of the matrix, respectively, and μ is fluid viscosity. Porosity decreases due to crystallization as the melt enters the TBL, allowing fluid pressure to increase and potentially decompacting the matrix. The time scale over which decompaction occurs is expressed as:

$$\tau_v = \frac{\delta_c}{w}, \tag{6}$$

where τ_ν is the matrix deformation time scale, δ_c is the compaction length, and w is the porous flow rate [*McKenzie*, 1984]. By contrast, crystallization occurs over a time scale of:

$$\tau_c = \left(w\frac{dT}{dz}\frac{df}{dT}\right)^{-1}, \tag{7}$$

where τ_c is the crystallization time scale, T is temperature, z is depth, and f is the equilibrium melt fraction [*Korenaga and Kelemen*, 1997]. The melt fraction is different from the porosity, which is influenced by decompaction and appears limited to 2% although f may approach 20% [*Grove et al.*, 1992; *Langmuir et al.*, 1992; *Spiegelman*, 1993c; *The MELT Seismic Team*, 1998].

[18] If $\tau_\nu \geq \tau_c$, the matrix cannot deform fast enough to keep the pore space open and a melt impermeable barrier may form [*Korenaga and Kelemen*, 1997]. Thus, a permeability barrier may develop if the decompaction time scale exceeds the crystallization time scale. Equivalently, by combining equations (6) and (7), it is clear that permeability barriers will develop if the actual compaction length is larger than a critical compaction length δ_c*.

$$\delta_c \geq \delta_c^*, \quad \text{with} \quad \delta_c^* = \left(\frac{dT}{dz}\frac{df}{dT}\right)^{-1}, \tag{8}$$

Note that δ_c* does not depend on the melt velocity and that, as we consider that z increases downward, δ_c* is a positive number, as is physically reasonable.

[19] In our analysis, we monitor the mass M that remains from a batch of melt formed at P_F, as a function of pressure in the form of the change in crystallinity measured in weight percent over the change in pressure measured in bars (dM/dP). A higher value for dM/dP reflects a higher crystallization rate over a sharper depth interval, and the maximum value in each column, $(dM/dP)_{\max}$, serves as a proxy for the strength of the crystallization front. Therefore, a high $(dM/dP)_{\max}$ is a necessary prerequisite for development of a permeability barrier and consequently lateral melt migration along the base of that barrier, in agreement with results by *Spiegelman* [1993c]. We consider that a permeability barrier forms at a crystallization rate that satisfies:

$$\left(\frac{dM}{dP}\right)_{\max}^{column} \geq \left(\frac{dM}{dP}\right)^* \propto \frac{1}{\delta_c^*}, \tag{9}$$

As the driving force of lateral melt migration toward to the axis is the melt buoyancy resolved along the permeability barrier, we take into consideration the slope of the proposed barrier as a potential limitation for melt focusing.

[20] In section 3, we report values of $(dM/dP)_{\max}$ and discuss the crystallization sequence as a function of distance from the axis for various spreading rates.

3. Results

3.1. Defining the Crystallization Front

[21] Vertical melt pathways at different distances off axis produce different crystallization behaviors. This is due to both the change in composition of the melts with distance from the axis (due to the shortening melting column) as well as the increasing TBL thickness. As ascending melts enter the TBL, partial melting gives way to partial crystallization, assuming complete thermal equilibration of the transiting melts with the ambient temperature structure. Typically, crystallization is slow at depth, but increases sharply when multiple saturation is achieved (Figure 3a).

[22] This standard behavior dominates the crystallization sequence at the fastest spreading ridge case (U_0 = 100 mm/yr) (Figure 3b), especially close to the axis. We observe the highest values of dM/dP

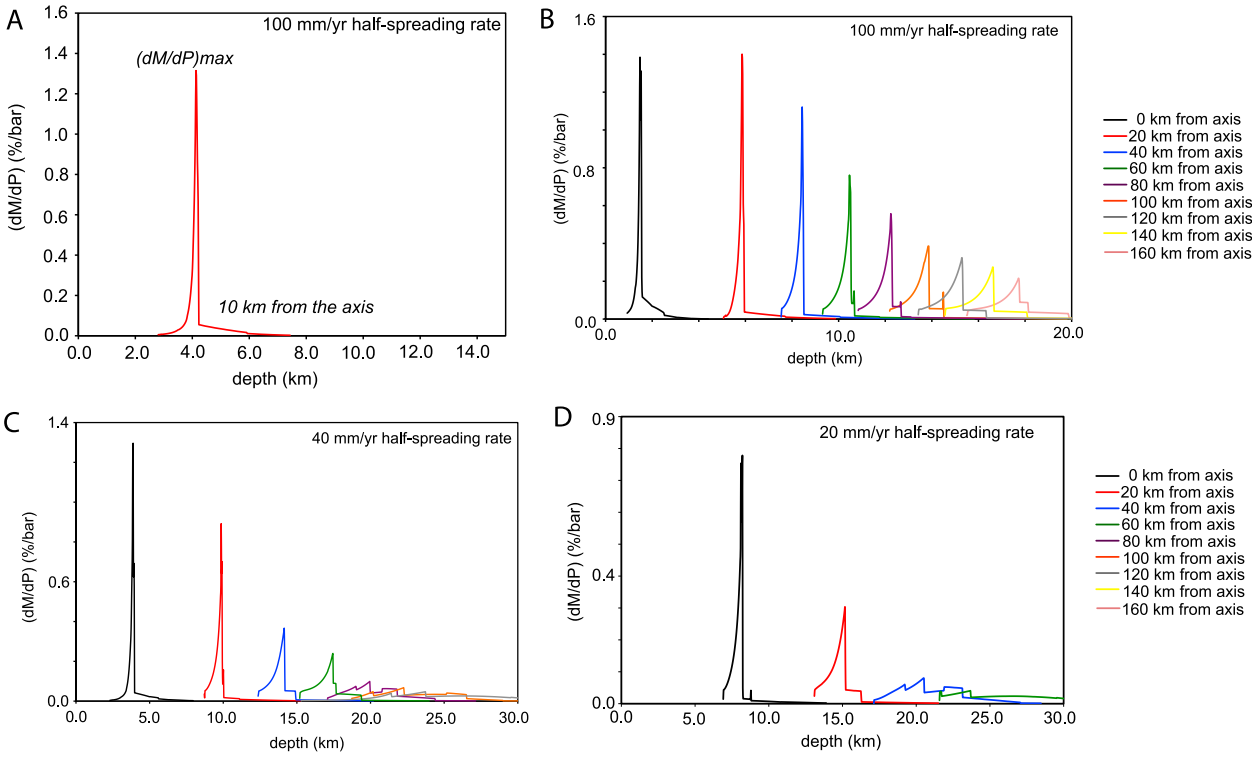

Figure 3. Crystallization rate dM/dP versus depth for vertical melt trajectories at different distances off axis: (a) a single melt trajectory at 10 km off axis for a fast spreading case (U_0 = 100 mm/yr). In this example, dM/dP is maximum at 4 km depth. (b) dM/dP for different distances off axis for a fast spreading case (U_0 = 100 mm/yr). (c) dM/dP at different distances off axis for an intermediate spreading case (U_0 = 40 mm/yr). (d) dM/dP at different distances off axis for a slow spreading case (U_0 = 20 mm/yr). Note the different scales.

along vertical melt columns closest to the axis where plagioclase and clinopyroxene become stable around the same depth, combining to generate a large burst of crystallization over a short pressure interval. Further from the axis, the pressures at which plagioclase-in and clinopyroxene-in occur diverge as the TBL thickens. This contributes to decreasing values of $(dM/dP)_{max}$ with increasing distance away from the axis.

[23] As spreading rate decreases, the maximum crystallization rate, $(dM/dP)_{max}$, decreases throughout the ridge system, but the highest values are still associated with near-axis vertical trajectories. This is a consequence of the thickness of the TBL, which increases significantly both with distance from the axis, and with decreasing spreading rate. Phase identity associated with $(dM/dP)_{max}$ for a slow to intermediate spreading rate case (U_0 = 40 mm/yr, Figure 3c) are plagioclase + clinopyroxene for vertical trajectories up to 22 km off axis and plagioclase alone for trajectories >22 km, where clinopyroxene-in appears as a secondary peak in dM/dP. With increasing distance from the axis, values of $(dM/dP)_{max}$ continue to decrease, and the strong single peak associated with plagioclase-in changes to a more bimodal distribution as the pattern of crystallization (a function of the geothermal gradient) changes with the addition of a broad spinel-in peak comparable in amplitude with the plagioclase-in peaks.

[24] For slow to ultraslow spreading cases ($U_0 \leq$ 20 mm/yr, Figure 3d), values of $(dM/dP)_{max}$ occur at relatively greater depths and values for $(dM/dP)_{max}$ are significantly less than those calculated at similar off-axis distances at higher spreading rates. In all model cases, the depth of the maximum crystallization rate increases and its value decreases away from the axis.

[25] At all spreading rates, the locus of $(dM/dP)_{max}$ is shallowest underneath the ridge axis, but it deepens progressively with decreasing spreading rate, from within the crust for $U_0 \geq 20$ mm/yr to mantle depths for slow to ultraslow models (Figure 4).

3.2. Geometry of the Permeability Barrier

[26] We infer the presence of a crystallization front at the position of $(dM/dP)_{max}$ gleaned from thermal

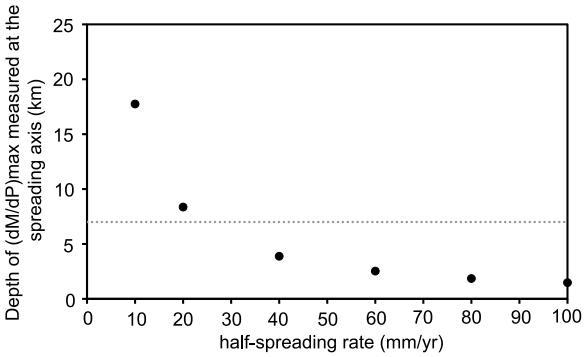

Figure 4. Depth of the maximum crystallization rate $(dM/dP)_{max}$ versus half-spreading rate, measured underneath the ridge axis. The dotted gray line depicts the average depth of oceanic crust.

and chemical modeling and associated primarily with the appearance of plagioclase in the crystallizing assemblage. The crystallization front slopes downward from the spreading center, which is a necessary prerequisite for buoyancy-driven melt migration toward the ridge. However, melt focusing depends also on the slope of the barrier that may form at the crystallization front.

[27] In order to determine reasonable limits on the extent of the permeability barrier with regard to geochemical and seismic data sets, we perform crustal thickness calculations with limits imposed on melt focusing associated with the slope of the crystallization front and compare with actual data collected as a function of spreading rate (Figure 5). Crustal thickness (H_C) is crudely approximated by:

$$H_C = \frac{1}{V}\int_0^{x_e}\int_{z_s}^{z_F} v_z \frac{\partial F}{\partial z}\, dz\, dx, \qquad (10)$$

where V is the effective spreading rate, v_z is the vertical component of velocity, $\partial F/\partial z$ is the melt productivity, z_s and z_F are the depths of the solidus and F_{max}, which bound the active melting region (Figure 1), and x_e is the lateral extent of the extraction zone, measured to correspond to a particular limit on the slope of the crystallization front defined by $(dM/dP)_{max}$.

[28] We limit the extraction zone such to collect melt only if the slope of the permeability barrier (if it exists) is larger than a critical value. Melt migrates toward the axis under the influence of buoyancy. If the slope of the permeability barrier is too small, the magnitude of the buoyancy force resolved along the barrier is too small to induce significant melt migration toward the axis. Adopting a critical slope of −0.05 to −0.10 leads to crustal thicknesses comparable to observations for spreading rates ≥ 40 mm/yr half rate (Figure 5, black and blue lines). For all model cases, as distance from the axis increases, the slope of the crystallization front decreases. However, for a value of the slope greater than −0.05 and for $U_0 \geq 40$ mm/yr, the width of the extraction zone decreases as spreading rate increases. This

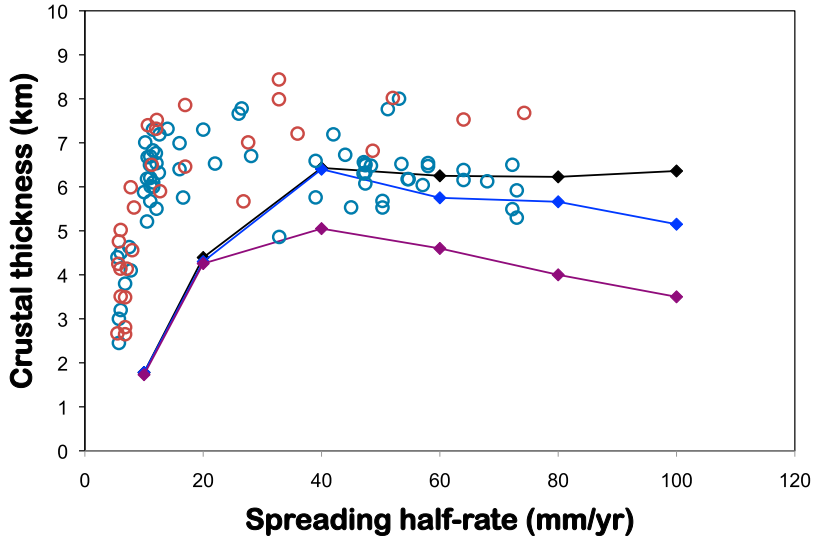

Figure 5. Crustal thickness from seismic observations and rare earth element inversions compiled by *White et al.* [2001] (blue and red open circles, respectively) and from our model for various spreading rates (connected diamonds, equation (10)). Each curve corresponds to a minimum slope of the permeability barrier needed to allow melt extraction: −0.15 (purple), −0.10 (blue), or −0.05 (black). The crustal thickness compilation does not include results from fracture zones, marginal basins, or locations associated with plumes [*White et al.*, 2001].

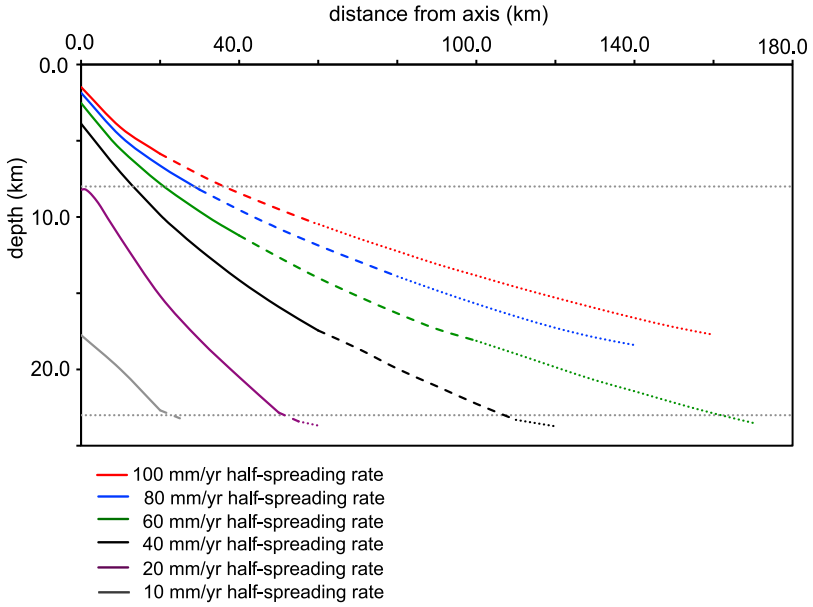

Figure 6. Depth of the crystallization front defined by $(dM/dP)_{max}$ versus off-axis distance for various spreading rates. The two dotted gray lines limit the region where equation (1) describes the temperature of the permeability barrier within 10°C. The slope of the barrier is more than 0.15 where the lines are solid, between 0.1 and 0.15 where the lines are dashed, and between 0.05 and 0.1 where the lines are dotted.

effect can be stronger than the overall increase in melt production due to a generally thinner TBL at fastest spreading rates, and could explain why the thickest crusts are not observed at the fastest ridges (Figure 4) [*White et al.*, 2001]. For spreading rates $\leq$ 20 mm/yr, our model underpredicts crustal thickness compared with observations. Additionally, the lowest values for $(dM/dP)_{max}$ are seen at the lowest spreading rates, indicating a weaker crystallization front. In these cases, melt focusing to the axis may occur due to an alternative mechanism.

[29] Given our crustal thickness analysis, it is appropriate to set a value for the critical slope to be approximately −0.05 in order to define an effective permeability barrier, such that the slope of $(dM/dP)_{max}$ with distance off axis must exceed the critical value in order for melt to migrate. In addition, the crystallization rate associated with this critical slope must exceed the threshold value to form a permeability barrier, $(dM/dP)^*$, which is related to the compaction length (equation (8)). For the model case where U_0 = 10 mm/yr, the value for $(dM/dP)_{max}$ at x_e corresponding to the slope = −0.05 is 0.03 wt. %/bar. For all faster spreading model cases, $(dM/dP)_{max}$ at x_e exceeds 0.03. Thus, we choose 0.03 wt. %/bar as an upper estimate of $(dM/dP)^*$. The critical compaction length, δ_c^*, corresponding to $(dM/dP)^*$ is ~10 km. Even though the strength of the crystallization front, measured by $(dM/dP)_{max}$, may be greater than $(dM/dP)^*$ beyond x_e for the faster spreading cases, the limitation on the slope prevents focusing along the permeability barrier. Beyond x_e, melts would stall in melt ponds along the barrier and would be advected further off axis, where they cool and crystallize.

[30] The permeability barrier is now defined by the sloping crystallization front within the TBL, and is limited in its lateral extent by a value for the critical slope of that crystallization front, as well as the relative strength of the crystallization front (Figure 6). As spreading rates decrease, the TBL is thicker, and the permeability barrier is correspondingly deeper. Due to the restriction on the slope, the permeability barrier is no longer effective when the maximum crystallization rate $(dM/dP)_{max}$ is encountered deeper than ~24 km regardless of the spreading rate. The sudden change in slope of the crystallization front at ~24 km depth of every spreading rate is related to the crystallization sequence.

[31] *Montési and Behn* [2007] proposed a simple relation between the temperature and depth of a permeability barrier (equation (1)). This relation proposed is based on the association of a melt permeability barrier with the plagioclase multiple saturation point, determined at 1240°C at the base of the crust by *Kelemen and Aharonov* [1998], with a pressure correction following the experimental

work of *Yang et al.* [1996]. The temperatures given by this relation can be assessed relative to the temperature at $(dM/dP)_{max}$ (associated mostly with plagioclase-in) calculated for the different melting columns with distance away from the axis for the model cases. In general, equation (1) provides a valid approximation (within ±10°C) to the location of $(dM/dP)_{max}$ where there is an effective permeability barrier within the subcrustal range of 8–23 km. This interval describes where plagioclase begins to crystallize at depths > 8 km to the lateral extent of the barrier where $(dM/dP)_{max} < (dM/dP)^*$, defined by the critical slope. Equation 1 is less appropriate at ultraslow spreading rates (U_0 < 10 mm/yr), where the TBL is thick and the crystallization front is weak. In summation, equation 1 is a valid representation for the position of the permeability barrier at subcrustal depths for $U_0 \geq 10$ mm/yr (Figure 6), where the crystallization front is shallower than approximately 23 km.

4. Discussion

[32] We solved for the thermal field and flow structure of MOR spreading centers with spreading rates ranging from fast to ultraslow. We used a petrological algorithm, MELTS, to solve for melting and crystallization behavior based on vertical melt migration beneath the TBL at different distances from the spreading axis. We evaluated the presence or absence of an effective melt permeability barrier, which may allow for lateral melt migration toward the neovolcanic zone, based on the strength of a crystallization front, defined by the quantity $(dM/dP)_{max}$ and a critical slope necessary for realistic crustal production. Now we discuss observations that can be used to evaluate the success of this permeability barrier model.

4.1. Crystallization Within a TBL

[33] As spreading rate decreases, the presence of the thick, conductively cooled TBL has a profound impact on the crystallization behavior of melts transiting the layer. We argued that an effective permeability barrier, requiring fairly rapid crystallization over a short depth interval, is associated with $(dM/dP)_{max}$ exceeding 0.03 wt. %/bar. This crystallization rate corresponds to a critical compaction length, δ_c^*, on the order of 10 km. The actual compaction length δ_c must be larger than δ_c^* for a permeability barrier to form. *Rabinowicz and Ceuleneer* [2005] infer an interval of 150–1500 m for the compaction length, given a melt viscosity of 1 to 100 Pa s [*Kushiro*, 1986] and a grain size of ~3 mm, but the compaction length might reach 10 km in conduits of focused flow within rocks with an average grain size larger than 4 mm [*Kelemen et al.*, 1997]. *Katz* [2008] argues that compaction lengths may be a factor of 10 higher than standard estimates as the bulk viscosity is inversely proportional to porosity [see also *Schmeling*, 2000; *Simpson et al.*, 2010]. These estimates are compatible with the critical value suggested by our analysis.

[34] *Herzberg* [2004] calculated pressures of partial crystallization for a global MOR basalt glass database using various parameterizations of experimental data sets. He concluded that MORB from fast spreading ridges underwent partial crystallization only within the crust while MOR basalt from slow spreading centers started to crystallize at mantle depths. These conclusions are in agreement with the results of *Michael and Cornell* [1998], who also explored correlations between pressure of crystallization and spreading rate, and with other studies that emphasized the importance of higher-pressure crystallization to MOR basalt petrogenesis at slower spreading ridges [*Grove et al.*, 1992; *Yang et al.*, 1996; *Danyshevsky et al.*, 1996; *Villiger et al.*, 2007]. Estimates for the top of the partial melting region were deeper than about 25–30 km below slow spreading centers [*Herzberg*, 2004]. *Shaw et al.* [2010] report evidence for melt pooling and crystallization at 9–20 km depth based on analyses of melt inclusions collected at the ultraslow spreading Gakkel ridge.

[35] Our model implies that crystallization will start slightly below the permeability barrier. Figures 4 and 6 imply partial crystallization at mantle depths possibly greater than 20 km at slow and ultraslow spreading centers, in agreement with the studies mentioned above. In our model, as in these observations, the maximum crystallization rate is found at crustal depths at spreading rates larger than 25 mm/yr half rate (Figure 4), which agrees with the conclusions of *Herzberg* [2004] and *Michael and Cornell* [1998]. However, *Lissenberg and Dick* [2008] proposed an alternative explanation for the greater crystallization pressures associated with slower spreading ridges whereby melt-rock reaction by an assimilation/fractional crystallization (AFC) process in the crust may contribute to the spread of MOR basalt compositions and shifts in melt composition toward lower CaO and SiO_2 and higher Al_2O_3 and MgO previously attributed to partial crystallization at mantle depths. It remains that the depth of conductive cooling increases as a function of spreading rate and influences strongly the initia-

tion of crystallization. Thus, crystallization at mantle depths cannot be avoided at slow and ultraslow ridges, whether or not it is the correct explanation of the MORB glass systematics described by *Michael and Cornell* [1998], *Herzberg* [2004], and others.

4.2. Predicted Crustal Thickness

[36] A test of our model is provided by the variation in crustal thickness versus spreading rate (Figure 5). Oceanic crust is generally 6 to 8 km thick, with little dependence on spreading rate. Only for spreading rates less than 10 mm/yr (half rate) is there a decrease in crustal thickness [e.g., *White et al.*, 2001]. However, this decrease is so rapid that crust-free areas appear at spreading rate less than 6 mm/yr [*Dick et al.*, 2003; *Michael et al.*, 2003]. Interestingly, the thickest crust in the compilation by *White et al.* [2001] is found at an intermediate spreading rate of 32.8 mm/yr, half rate, roughly coincident with the increased crustal thickness seen for U_0 = 40 mm/yr relative to faster spreading model cases (Figure 5).

[37] The permeability barrier geometry, limited by a critical slope, suggests a way to focus the majority of melt produced beneath the ridge toward the spreading axis, consistent with observations of crustal thickness, for spreading rates ≥ 40 mm/yr. Part of the melt may be lost because it rises at a location where the barrier is weak or its slope is too small to allow focusing. There, melt is absorbed by the lithosphere instead of being extracted to form the oceanic crust. *Gregg et al.* [2009] followed a similar concept with an extraction zone of 75 km but with a cooler mantle temperature (1325°C) to model crustal thickness. Their melting model is also similar to that used here. However, they did not consider whether a permeability barrier is strong enough to form a decompaction channel, as we do here, and they did not provide a physical justification for a constant width of the melt extraction zone. Here, we link the extraction zone with the slope of the permeability barrier and document systematic variations in the width of the extraction zone that a compatible with the observed crustal thickness systematics.

[38] It is notable that our model significantly underpredicts the crustal thickness at slow and ultraslow ridges. As we discuss in more detail in section 4.4, there must be an additional mechanism for efficiently extracting melts at slow spreading centers, whether associated with a permeability barrier or not.

4.3. Lateral Extent of the Permeability Barrier for $U_0 \geq 10$ mm/yr

[39] A strong crystallization front can produce a melt impermeable layer by rapidly reducing porosity and permeability. A condition relating the time scales of crystallization and deformation has been proposed to indicate the criterion for "clogging" the pore space to a degree necessary for the development of a permeability barrier ($\tau_\nu \geq \tau_c$) [*Korenaga and Kelemen*, 1997], resulting in a definition of a critical compaction length scale (δ_c^*) related to the degree of crystal fractionation over a change in depth (equation (8)). If the condition $\tau_\nu \geq \tau_c$ defines the existence of a permeability barrier, we can then determine the lateral extent of the barrier for the different model cases based on the strength and the slope of the crystallization front, measured by $(dM/dP)_{\max}$.

[40] As shown in Figure 6, a permeability barrier exists for $U_0 \geq 10$ mm/yr, and becomes generally more laterally extensive with an increasing spreading rate, sloping outward and down from the ridge axis as a function of the changing thermal profile. It is significant that the barrier is not at a constant depth for each spreading rate model case. The overall slope of the impermeable surface also shallows with increasing distance from the axis, most notably for the fastest spreading rates where the barrier is more extensive. This may mean that lateral melt transport to the axis along a melt impermeable surface will exist, but the less steep lithospheric wedge angle may inhibit strong focusing from greater distances off axis. As was discussed in section 4.2, limiting melt transport by a critical slope of roughly −0.05 results in reasonable crustal thickness at spreading rates greater than or equal to 40 mm/yr half rate.

[41] *Sohn and Sims* [2005] hypothesized that bending stresses could trigger off-axis volcanism at the East Pacific Rise, a fast spreading ridge, by opening downward propagating cracks and tapping melt bodies in the lower crust potentially emplaced along a permeability barrier. The presence of a permeability barrier to considerable lateral extents below fast spreading ridges indicates that there may be significant fractions of melt either stalled at the melt impermeable boundary or traveling toward the axis along the base of the boundary. The relatively low slope of the barrier for the fast spreading case implies that the former is more likely.

[42] Direct geophysical evidence for off-axis melt accumulation at fast and intermediate spreading centers is available. *Garmany* [1989] reported

strong *P* to *S* conversion at the Moho 22 km off axis from the EPR at several locations between 12°N and 12°50′N. This observation is consistent with our prediction of the off-axis distance for which the permeability barrier is at the base of the crust (Figure 6). Partial melt was also observed in the lower crust and localized sills at the Moho for the EPR at 9°48′N, based on seafloor compliance measurements [*Crawford et al.*, 1999; *Crawford and Webb*, 2002]. Melt accumulation zones were detected to a least 10 km off axis, where their top was approximately 4 km beneath the seafloor, again in rough agreement with our predicted geometry of the permeability barrier at fast spreading rates (Figure 6).

[43] At the Juan de Fuca Ridge, where the spreading rate is intermediate, seismic reflection surveys revealed possible melt accumulation zone in the lower crust off axis as well. Clear melt sills are detected at 5–6 km beneath the seafloor (850–900 m above the Moho) from 1.4 to 3.2 km off axis [*Canales et al.*, 2009]. Anomalously thick mantle transition zones are imaged 20 km off axis. They feature gabbroic sills slightly below the Moho [*Nedimović et al.*, 2005], in the vicinity of the crossover between our permeability barriers and the Moho (Figure 6). Thus, the geometry of the permeability barrier inferred from our model is consistent not only with geochemical evidence of crystallization depth (see section 4.1) but geophysical evidence for off-axis melt sills.

4.4. Melt Focusing Beneath Ultraslow Ridges: A Different Mechanism?

[44] *Montési and Behn* [2007] presented an analytical solution for mantle flow beneath an oblique ridge, demonstrating that the thermal structure and crustal thickness are controlled by the effective spreading rate. Using a simple relationship (equation (1)) that estimates the lithospheric thickness by calculating the depth-corrected temperature of plagioclase saturation, *Montési and Behn* [2007] provide a correlation between the effective spreading rate and the estimated lithospheric thickness, predicting a permeability barrier that reaches depths of ~30 km at the slow/ultraslow transition. They conclude that the transition from slow to ultraslow spreading is related to a change in the efficiency of vertical melt extraction due to reduced melt volume and thicker lithosphere.

[45] At ultraslow spreading rates, however, the high TBL thickness results in very low values of $(dM/dP)_{max}$ independent of distance from axis, indicating a weak crystallization front and precluding the development of a permeability barrier, according to our model. The protracted crystallization history of migrating melts through the thick TBL associated with slow to ultraslow spreading rates may allow melt to be preferentially incorporated into the lithospheric mantle, explaining the dearth of volcanism at ultraslow ridges [*Chen*, 1992; *Cannat*, 1996; *Dick et al.*, 2003; *Montési and Behn*, 2007]. The process of melt incorporation would refertilize the lithospheric peridotite, which may lead to lithological heterogeneity, such as observed in eclogite and pyroxenite veins within alpine peridotite massifs and discussed by *Herzberg* [2004]. *Lizarralde et al.* [2004] present results from a seismic refraction survey describing significant changes in mantle velocity gradient, basement topography, and crustal thickness that correspond closely with a change from slow to ultraslow rates and are explained by variations in melt extraction at the ridge. Due to the increased effect of conductive cooling at the slower spreading rates, more melt is retained within the mantle as a gabbroic phase [*Lizarralde et al.*, 2004]. *Drouin et al.* [2010] present compositional and microstructural analysis of olivine-rich troctolites from the slow spreading Mid-Atlantic Ridge (30°N) and conclude that while there is a lack of volcanism associated with the section, magmatic activity was high, and that most of the melt may have been trapped in the lithosphere. Additionally, the lack of a permeability barrier may result in an increased tendency for off-axis volcanism to play a nontrivial role in crustal accretion at ultraslow ridges. *Standish and Sims* [2010] report effectively zero-age lava up to 10 km off axis at the ultraslow 9°E–25°E section of the SWIR, implying widely dispersed volcanism.

[46] Our model predicts that a transition from focused to distributed volcanism accompanied by lithospheric refertilization occurs for spreading rates below U_0 = 10 mm/yr. The transition was defined at 10 mm/yr based on crustal thickness data [*Dick et al.*, 2003; *Cannat et al.*, 2006] while *Montési and Behn* [2007] selected 6.5 ± 0.3 mm/yr based on the lack of continuous volcanism at ultraslow spreading. In addition, stronger melt focusing than predicted by our model must be in effect to explain crustal thickness of slow ridges (Figure 5). Melt focusing has been invoked to explain geochemical systematics and crustal variations at the SWIR 9°E–16°E area [*Standish et al.*, 2008]. To form a permeability barrier according to our model requires a critical compaction length of

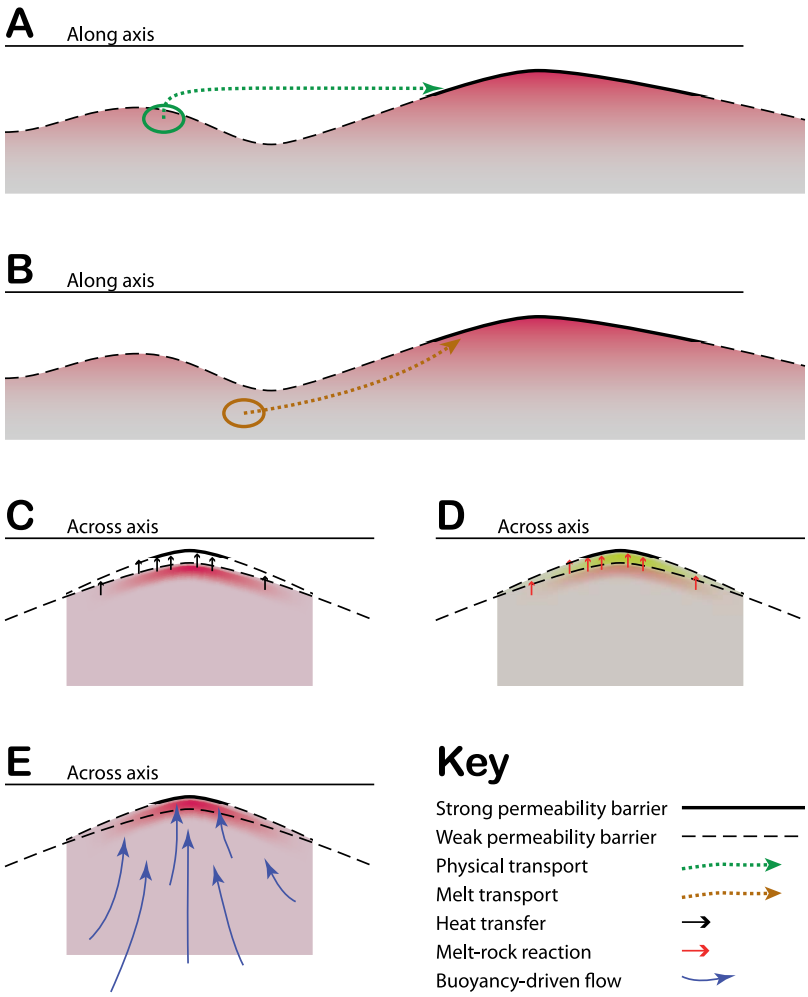

Figure 7. Cartoons showing potential alternative mechanisms for lateral melt transport beneath ultraslow spreading ridges. Melt accumulation is represented by stronger shades of pink, and melt-rock reactions are represented by strong shades of yellow in Figure 7d (overlapping with the pink). (a) Melts from the ultraslow oblique segment freeze in the lower lithosphere and advect away as heterogeneities (green arrow) until they may be incorporated in the melting region of adjacent magmatic segment, where a faster effective spreading rate allows for a more extensive melting region. (b) Melts from the edge of the melting region of an ultraslow oblique segment may become entrained in the drainage network associated with an adjacent magmatic segment. (c) Melts freezing in the lithosphere release latent heat, which erodes the TBL. (d) Melts react with surrounding solid rocks, increasing melt flux and retarding crystallization. (e) Buoyancy-driven flow at the spreading center brings hot material and erodes the TBL. The mechanisms in Figures 7c–7e use local processes to retard crystallization to shallower depth where a melt impermeable boundary may form, whereas the mechanisms in Figures 7a and 7b rely on mass transfer from one segment to another.

at least 10 km, at the high end of published estimates [*Kelemen et al.*, 1997; *Katz*, 2008]. Thus, we suspect that an alternative mode of melt focusing is acting at slow and possibly ultraslow spreading centers.

[47] While this study does not address any of these mechanisms in details, we can propose several possible hypotheses for the lateral focusing of melt toward and along the axes of ultraslow spreading ridges (Figure 7). We place particular emphasis on the SWIR geometry, where geochemical enrichments perhaps indicate a contribution from deeply originating, low-F melts from beneath amagmatic segments to adjacent magmatic segments [*Standish et al.*, 2008].

[48] In the presence of a complex flow field, or if the geometry of the ridge axis changes rapidly [*Cannat et al.*, 2006], melts trapped in the thick TBL of ultraslow ridges at amagmatic segments may become entrained with the solid flow field spreading away from the axis and may become subsequently eroded and incorporated into the

melting region of the neighboring magmatic segment (Figure 7a), serving as mantle heterogeneities and manifesting themselves at the ridge axis as chemical enrichments [*Cannat et al.*, 2008]. This model can be tested in regions where short-lived changes in spreading geometry are associated with crustal thickness differences, such as the eastern tip of the SWIR [*Cannat et al.*, 2006], as these changes in crustal thickness are most likely to remelt a pocket of refertilized lithosphere. An alternative possibility is that melts from the edges of the amagmatic segments will become entrained in the drainage network associated with the adjacent magmatic segment (Figure 7b), resulting in peripheral enrichments. Melts that rise from the melting region beneath the ultraslow spreading ridge may freeze into the lower part of the lithosphere, releasing latent heat and perturbing the thermal structure and resulting in erosion of the TBL and a narrowing of the depth interval over which crystallization occurs (Figure 7c). The crystallization sequence may be perturbed by assimilation of wall rock (Figure 7d), which could increase crystallization [*Kelemen and Aharonov*, 1998]. Melt-rock reaction has been documented at the slow to ultraslow spreading SWIR [*Seyler et al.*, 2007; *Warren et al.*, 2009; *Warren and Shimizu*, 2010] and at ophiolites of inferred slow to ultraslow ridges [*Müntener et al.*, 2010]. Finally, diapiric instabilities (Figure 7e) are expected to be more dominant at slower spreading rate [*Lin and Phipps Morgan*, 1992], and may take over as origin of focusing at ultraslow spreading [*Cannat et al.*, 2008], although they appear less efficient than permeability barriers at focusing melt at the slow spreading Mid-Atlantic Ridge [*Magde and Sparks*, 1997]. Diapiric instabilities, effects of latent heat of crystallization, and melt-rock reaction would all delay crystallization, thin the TBL, and increase the likelihood of development of a permeability barrier.

5. Conclusions

[49] Spreading rate impacts the thermal structure beneath the ridge, resulting in the possibility of different crystallization behavior of vertically migrating melts as a function of distance from the axis. Permeability barriers may exist beneath slow to fast spreading ridges ($U_0 \geq 10$ mm/yr), with the lateral extent of the barrier from the axis generally decreasing as spreading rate decreases. Despite the wider extent, the shallower lithospheric slope seen in faster spreading ridges may impede lateral focusing of melt along the permeability barrier compared to slower spreading ridges. Forming permeability barriers at ultraslow spreading ridges ($U_0 < 10$ mm/yr) is more difficult, due to the thick conductive lid and lack of a strong crystallization front, leading to the suspicion that other mechanisms and feedback processes are required for lateral melt focusing.

Acknowledgments

[50] This work was supported by NSF grant OCE-0649103. We would like to gratefully acknowledge reviews by Claude Herzberg and an anonymous reviewer. L.G.J.M. also thanks Mark Behn, Henry Dick, Peter Kelemen, and Marc Spiegelman for numerous discussions on the mechanisms of melt extraction at mid-ocean ridges; Trish Gregg, Jessica Warren, and Jeff Standish for discussion of their results in advance of publication; and Bob White for sharing his compilation of crustal thicknesses with us.

References

Aharonov, E., J. A. Whitehead, P. B. Kelemen, and M. Spiegelman (1995), Channeling instability of upwelling melt in the mantle, *J. Geophys. Res.*, *100*, 20,433–20,450, doi:10.1029/95JB01307.

Asimow, P. D., and M. S. Ghiorso (1998), Algorithmic modifications extending MELTS to calculate subsolidus phase relations, *Am. Mineral.*, *83*(9–10), 1127–1132.

Asimow, P. D., and C. H. Langmuir (2003), The importance of water to oceanic melting regimes, *Nature*, *421*, 815–820, doi:10.1038/nature01429.

Asimow, P. D., and E. M. Stolper (1999), Steady-state mantle-melt interactions in one dimension: I. Equilibrium transport and melt focusing, *J. Petrol.*, *40*(3), 475–494, doi:10.1093/petrology/40.3.475.

Baker, M. B., M. M. Hirschmann, M. S. Ghiorso, and E. M. Stolper (1995), Compositions of low-degree partial melts of peridotite: Results from experiments and thermodynamic calculations, *Nature*, *375*, 309–311.

Batchelor, G. (1967), *An Introduction to Fluid Dynamics*, 615 pp., Cambridge Univ. Press, Cambridge, U. K.

Bown, J. W., and R. S. White (1994), Variation with spreading rate of oceanic crustal thickness and geochemistry, *Earth Planet. Sci. Lett.*, *121*, 435–449, doi:10.1016/0012-821X(94)90082-5.

Buck, W. R., and W. Su (1989), Focused mantle upwelling below MORs due to feedback between viscosity and melting, *Geophys. Res. Lett.*, *16*, 641–644, doi:10.1029/GL016i007p00641.

Canales, J. P., M. R. Nedimović, G. M. Kent, S. M. Carbotte, and R. S. Detrick (2009), Seismic reflection images of a near-axis melt sill within the lower crust at the Juan de Fuca ridge, *Nature*, *460*, 89–93, doi:10.1038/nature08095.

Cannat, M. (1996), How thick is the magmatic crust at slow spreading oceanic ridges?, *J. Geophys. Res.*, *101*, 2847–2857, doi:10.1029/95JB03116.

Cannat, M., et al. (1995), Thin crust, ultramafic exposures, and rugged faulting patterns at the Mid-Atlantic Ridge (22°–24°N), *Geology*, *23*, 49–52, doi:10.1130/0091-7613(1995)023<0049:TCUEAR>2.3.CO;2.

Cannat, M., D. Sauter, V. Mendel, E. Ruellan, K. Okino, J. Escartin, V. Combier, and M. Baala (2006), Modes of seafloor generation at a melt-poor ultraslow-spreading ridge, *Geology*, *34*(7), 605–608, doi:10.1130/G22486.1.

Cannat, M., D. Sauter, A. Bezos, C. Meyzen, E. Humler, and M. Le Rigoleur (2008), Spreading rate, spreading obliquity, and melt supply at the ultraslow spreading Southwest Indian Ridge, *Geochem. Geophys. Geosyst.*, *9*, Q04002, doi:10.1029/2007GC001676.

Ceuleneer, G., and M. Rabinowicz (1992), Mantle flow and melt migration beneath oceanic ridges, in *Mantle Flow and Melt Generation at MORs*, *Geophys. Monogr. Ser.*, vol. 71, edited by J. Phipps Morgan, D. K. Blackman, and J. M. Sinton, pp. 123–154, AGU, Washington, D. C.

Chen, Y. J. (1992), Oceanic crustal thickness versus spreading rate, *Geophys. Res. Lett.*, *19*(8), 753–756, doi:10.1029/92GL00161.

Crawford, W. C., and S. C. Webb (2002), Variations in the distribution of magma in the lower crust and at the Moho beneath the East Pacific Rise at 9°–10°N, *Earth Planet. Sci. Lett.*, *203*, 117–130, doi:10.1016/S0012-821X(02)00831-2.

Crawford, W. C., S. C. Webb, and J. A. Hildebrand (1999), Constraints on melt in the lower crust and Moho at the East Pacific Rise, 9°48′N, using seafloor compliance measurements, *J. Geophys. Res.*, *104*, 2923–2939, doi:10.1029/1998JB900087.

Danyshevsky, L. V., A. V. Sobolev, and L. V. Dmitriev (1996), Estimation of the pressure of co-crystallization and H_2O content of MORB glasses: Calibration of an empirical technique, *Mineral. Petrol.*, *57*, 185–204, doi:10.1007/BF01162358.

Dick, H. J. B., J. Lin, and H. Schouten (2003), An ultraslow-spreading class of ocean ridge, *Nature*, *426*, 405–412, doi:10.1038/nature02128.

Drouin, M., B. Ildefonse, and M. Godard (2010), A microstructural imprint of melt impregnation in slow-spreading lithosphere: Olivine-rich troctolites from the Atlantis Massif, Mid-Atlantic Ridge, 30°N, IOD Hole U1309D, *Geochem. Geophys. Geosyst.*, *11*, Q06003, doi:10.1029/2009GC002995.

Dunn, R. A., V. Lekić, R. S. Detrick, and D. R. Toomey (2005), Three-dimensional seismic structure of the Mid-Atlantic Ridge (35°N): Evidence for focused melt supply and lower crustal dike injection, *J. Geophys. Res.*, *110*, B09101, doi:10.1029/2004JB003473.

Gaetani, G. A., T. L. Grove, and W. B. Bryan (1993), The influence of water on the petrogenesis of subduction-related igneous rocks, *Nature*, *365*, 332–334, doi:10.1038/365332a0.

Garmany, J. (1989), Accumulations of melt at the base of young oceanic crust, *Nature*, *340*, 628–632, doi:10.1038/340628a0.

Ghiorso, M. S., and R. O. Sack (1995), Chemical mass transfer in magmatic processes. 4. A revised and internally consistent thermodynamic model for the interpolation and extrapolation of liquid-solid equilibria in magmatic systems at elevated temperatures and pressures, *Contrib. Mineral. Petrol.*, *119*(2–3), 197–212, doi:10.1007/BF00307281.

Ghods, A., and J. Arkani-Hamed (2000), Melt migration beneath MORs, *Geophys. J. Int.*, *140*, 687–697, doi:10.1046/j.1365-246X.2000.00032.x.

Gregg, P. M., M. D. Behn, J. Lin, and T. L. Grove (2009), Melt generation, crystallization, and extraction beneath segmented oceanic transform faults, *J. Geophys. Res.*, *114*, B11102, doi:10.1029/2008JB006100.

Grove, T. L., R. J. Kinzler, and W. B. Bryan (1992), Fractionation of mid-ocean ridge basalt (MORB). Mantle flow and melt generation at mid-ocean ridges, in *Mantle Flow and Melt Generation at MORs*, *Geophys. Monogr. Ser.*, vol. 71, edited by J. Phipps Morgan, D. K. Blackman, and J. M. Sinton, pp. 281–310, AGU, Washington, D. C.

Hart, S. R. (1993), Equilibration during partial melting: A fractal tree model, *Proc. Natl. Acad. Sci. U. S. A.*, *90*, 11,914–11,918, doi:10.1073/pnas.90.24.11914.

Herzberg, C. (2004), Partial crystallization of MOR basalts in the crust and mantle, *J. Petrol.*, *45*(12), 2389–2405, doi:10.1093/petrology/egh040.

Hewitt, I. J., and A. C. Fowler (2008), Partial melting in an upwelling mantle column, *Proc. R. Soc. A*, *464*, 2467–2491, doi:10.1098/rspa.2008.0045.

Hirschmann, M. M., M. S. Ghiorso, L. E. Wasylenki, P. D. Asimow, and E. M. Stolper (1998), Calculation of peridotite partial melting from thermodynamic models of minerals and melts. I. Review of methods and comparison to experiments, *J. Petrol.*, *39*, 1091–1115, doi:10.1093/petrology/39.6.1091.

Hooft, E. E. E., R. S. Detrick, D. R. Toomey, J. A. Collins, and J. Lin (2000), Crustal thickness and structure along three contrasting spreading segments of the Mid – Atlantic Ridge, 33.5°–35°N, *J. Geophys. Res.*, *105*(B4), 8205–8226, doi:10.1029/1999JB900442.

Jull, M., P. B. Kelemen, and K. W. W. Sims (2002), Consequences of diffuse and channelized porous melt migration on uranium series disequilibria, *Geochim. Cosmochim. Acta*, *66*, 4133–4148, doi:10.1016/S0016-7037(02)00984-5.

Katz, R. F. (2008), Magma dynamics with the enthalpy method: Benchmark solutions and magmatic focusing at MORs, *J. Petrol.*, *49*(12), 2099–2121, doi:10.1093/petrology/egn058.

Katz, R. F., M. Spiegelman, and B. Holtzman (2006), The dynamics of melt and shear localization in partially molten aggregates, *Nature*, *442*, 676–679, doi:10.1038/nature05039.

Kelemen, P. B., and E. Aharonov (1998), Periodic formation of magma fractures and generation of layered gabbros in the lower crust beneath oceanic spreading ridges, in *Faulting and Magmatism at MORs*, *Geophys. Monogr. Ser.*, vol. 106, edited by W. R. Buck et al., pp. 267–289, AGU, Washington, D. C.

Kelemen, P. B., and H. J. B. Dick (1995), Focused melt flow and localized deformation in the upper mantle: Juxtaposition of replacive dunite and ductile shear zones in the Josephine peridotite, SW Oregon, *J. Geophys. Res.*, *100*, 423–438, doi:10.1029/94JB02063.

Kelemen, P. B., N. Shimizu, and V. J. M. Salters (1995a), Extraction of MOR basalt from the upwelling mantle by focused flow of melt in dunite channels, *Nature*, *375*, 747–753, doi:10.1038/375747a0.

Kelemen, P. B., J. A. Whitehead, E. Aharonov, and K. A. Jordahl (1995b), Experiments on flow focusing in soluble porous media, with applications to melt extraction from the mantle, *J. Geophys. Res.*, *100*, 475–496, doi:10.1029/94JB02544.

Kelemen, P. B., G. Hirth, N. Shimizu, M. Spiegelman, and H. J. B. Dick (1997), A review of melt migration processes in the adiabatically upwelling mantle beneath oceanic spreading ridges, *Philos. Trans. R. Soc. London, Ser. A*, *355*, 283–318, doi:10.1098/rsta.1997.0010.

Klein, E. M., and C. H. Langmuir (1987), Global correlations of ocean ridge basalt chemistry with axial depth and crystal thickness, *J. Geophys. Res.*, *92*, 8089–8115, doi:10.1029/JB092iB08p08089.

Korenaga, J., and P. B. Kelemen (1997), Origin of gabbro sills in the Moho transition zone of the Oman ophiolite: Implications for magma transport in the oceanic lower crust, *J. Geophys. Res.*, *102*(B12), 27,729–27,749, doi:10.1029/97JB02604.

Kushiro, I. (1986), Viscosity of partial melts in the upper mantle, *J. Geophys. Res.*, *91*, 9343–9350, doi:10.1029/JB091iB09p09343.

Langmuir, C. H., E. M. Klein, and T. Plank (1992), Petrological systematics of mid-ocean ridges basalts: Constraints on melt generation beneath ocean ridges, in *Mantle Flow and Melt Generation at MORs*, *Geophys. Monogr. Ser.*, vol. 71, edited by J. Phipps Morgan, D. K. Blackman, and J. M. Sinton, pp. 183–280, AGU, Washington, D. C.

Lin, J., and J. Phipps Morgan (1992), The spreading rate dependence of three-dimensional mid-ocean ridge gravity structure, *Geophys. Res. Lett.*, *19*, 13–16, doi:10.1029/91GL03041.

Lissenberg, C. J., and H. J. B. Dick (2008), Melt-rock reaction in the lower oceanic crust and its implications for the genesis of mid-ocean ridge basalt, *Earth Planet. Sci. Lett.*, *271*(1–4), 311–325, doi:10.1016/j.epsl.2008.04.023.

Lizarralde, D., J. B. Gaherty, J. A. Collins, G. Hirth, and S. D. Kim (2004), Spreading-rate dependence of melt extraction at mid-ocean ridges from mantle seismic refraction data, *Nature*, *432*, 744–747, doi:10.1038/nature03140.

Lundstrom, C. C., J. Gill, Q. Williams, and M. R. Perfit (1995), Mantle melting and basalt extraction by equilibrium porous flow, *Science*, *270*, 1958–1961, doi:10.1126/science.270.5244.1958.

Macdonald, K. C. (1982), Mid-ocean ridges: Fine scale tectonic, volcanic and hydrothermal processes within the plate boundary zone, *Annu. Rev. Earth Planet. Phys.*, *10*, 155–190, doi:10.1146/annurev.ea.10.050182.001103.

Magde, L. S., and D. W. Sparks (1997), Three-dimensional mantle upwelling, melt generation, and melt migration beneath segmented slow spreading ridges, *J. Geophys. Res.*, *102*(B9), 20,571–20,583, doi:10.1029/97JB01278.

Magde, L. S., D. W. Sparks, and R. S. Detrick (1997), The relationship between buoyant mantle flow, melt migration, and gravity bull's eyes at the Mid-Atlantic Ridge between 33°N and 35°N, *Earth Planet. Sci. Lett.*, *148*, 59–67, doi:10.1016/S0012-821X(97)00039-3.

McKenzie, D. (1969), Speculations on the consequences and causes of plate motions, *Geophys. J. R. Astron. Soc.*, *18*, 1–32.

McKenzie, D. (1984), The generation and compaction of partially molten rock, *J. Petrol.*, *25*, 713–765.

McKenzie, D. (1985), ^{230}Th-^{238}U disequilibrium and the melting processes beneath ridge axes, *Earth Planet. Sci. Lett.*, *72*, 149–157, doi:10.1016/0012-821X(85)90001-9.

Michael, P. J., and W. C. Cornell (1998), Influence of spreading rate and magma supply on crystallization and assimilation beneath MORs: Evidence from chlorine and major element chemistry of MOR basalts, *J. Geophys. Res.*, *103*, 18,325–18,356, doi:10.1029/98JB00791.

Michael, P. J., et al. (2003), Magmatic and amagmatic seafloor generation at the ultraslow-spreading Gakkel ridge, Arctic Ocean, *Nature*, *423*, 956–961, doi:10.1038/nature01704.

Montési, L. G. J., and M. D. Behn (2007), Mantle flow and melting underneath oblique and ultraslow MORs, *Geophys. Res. Lett.*, *34*, L24307, doi:10.1029/2007GL031067.

Müntener, O., G. Manatschal, L. Desmurs, and T. Pettke (2010), Plagioclase peridotites in ocean-continent transitions: Refertilized mantle domains generated by melt stagnation in the shallow mantle lithosphere, *J. Petrol.*, *51*, 255–294, doi:10.1093/petrology/egp087.

Nedimović, M. R., S. M. Carbotte, A. J. Harding, R. S. Detrick, J. P. Canales, J. B. Diebold, G. M. Kent, M. Tischer, and J. M. Babcock (2005), Frozen magma lenses below the oceanic crust, *Nature*, *436*, 1149–1152, doi:10.1038/nature03944.

Nicolas, A. (1990), Melt extraction from mantle peridotites: Hydrofracturing of porous flow consequences on oceanic ridge activity, in *Magma Transport and Storage*, edited by M. P. Ryan, pp. 160–174, John Wiley, Chichester, U. K.

Niu, Y., and R. Hékinian (1997), Spreading-rate dependence of the extent of mantle melting beneath ocean ridges, *Nature*, *385*, 326–329, doi:10.1038/385326a0.

Niu, Y., and M. J. O'Hara (2008), Global correlations of ocean ridge basalt chemistry with axial depth: A new perspective, *J. Petrol.*, *49*, 633–664, doi:10.1093/petrology/egm051.

Phipps Morgan, J. (1987), Melt migration beneath MOR spreading centers, *Geophys. Res. Lett.*, *14*, 1238–1241, doi:10.1029/GL014i012p01238.

Planert, L., E. R. Flueh, and T. J. Reston (2009), Along – and across – axis variations in crustal thickness and structure at the Mid-Atlantic Ridge at 5°S obtained from wide – angle seismic tomography: Implications for ridge segmentation, *J. Geophys. Res.*, *114*, B09102, doi:10.1029/2008JB006103.

Rabinowicz, M., and G. Ceuleneer (2005), The effect of sloped isotherms on melt migration in the shallow mantle: A physical and numerical model based on observations in the Oman ophiolite, *Earth Planet. Sci. Lett.*, *229*, 231–246, doi:10.1016/j.epsl.2004.09.039.

Rabinowicz, M., A. Nicolas, and J. Vigneresse (1984), A rolling mill effect in the asthenosphere beneath oceanic spreading centers, *Earth Planet. Sci. Lett.*, *67*, 97–108, doi:10.1016/0012-821X(84)90042-6.

Reid, I., and H. R. Jackson (1981), Oceanic spreading rate and crustal thickness, *Mar. Geophys. Res.*, *5*, 165–172.

Ribe, N. M. (1985), The generation and composition of partial melts in the Earth's mantle, *Earth Planet. Sci. Lett.*, *73*, 361–376, doi:10.1016/0012-821X(85)90084-6.

Ribe, N. M. (1988), On the dynamics of MORs, *J. Geophys. Res.*, *93*, 429–436, doi:10.1029/JB093iB01p00429.

Schmeling, H. (2000), Partial melting and melt segregation in a convecting mantle, in *Physics and Chemistry of Partially Molten Rocks*, edited by N. Bagdassarov, D. Laporte, and A. Thompson, pp. 141–178, Kluwer Acad., Dordrecht, Netherlands.

Scott, D., and D. Stevenson (1989), A self-consistent model of melting, magma migration, and buoyancy-driven circulation beneath MORs, *J. Geophys. Res.*, *94*, 2973–2988, doi:10.1029/JB094iB03p02973.

Seyler, M., J.-P. Lorand, H. J. B. Dick, and M.-P. Drouin (2007), Pervasive melt percolation reactions in ultra-depleted refractory harzburgites at the Mid-Atlantic Ridge, 15°20′N: ODP Hole 1274A, *Contrib. Mineral. Petrol.*, *153*, 303–319, doi:10.1007/s00410-006-0148-6.

Shaw, A. M., M. D. Behn, S. E. Humphris, R. A. Sohn, and P. M. Gregg (2010), Deep pooling of low degree melts and volatile fluxes at the 85°E segment of the Gakkel Ridge: Evidence from olivine-hosted melt inclusions and glasses, *Earth Planet. Sci. Lett.*, *289*, 311–322, doi:10.1016/j.epsl.2009.11.018.

Shen, Y., and D. W. Forsyth (1995), Geochemical constraints on initial and final depths of melting beneath MORs, *J. Geophys. Res.*, *100*, 2211–2237, doi:10.1029/94JB02768.

Simpson, G., M. Spiegelman, and M. I. Weinstein (2010), A multiscale model of partial melts: 2. Numerical results, *J. Geophys. Res.*, *115*, B04411, doi:10.1029/2009JB006376.

Sims, K. W. W., et al. (2002), Chemical and isotopic constraints on the generation and transport of magma beneath the East Pacific Rise, *Geochim. Cosmochim. Acta*, *66*, 3481–3504, doi:10.1016/S0016-7037(02)00909-2.

Sinton, J., and R. Detrick (1992), Mid-ocean ridge magma chambers, *J. Geophys. Res.*, *97*(B1), 197–216, doi:10.1029/91JB02508.

Sisson, T. W., and T. L. Grove (1993), Experimental investigations of the role of H_2O in calc-alkaline differentiation and subduction zone magmatism, *Contrib. Mineral. Petrol.*, *113*, 143–166, doi:10.1007/BF00283225.

Sleep, N. H. (1988), Tapping of melts by veins and dikes, *J. Geophys. Res.*, *93*, 10,255–10,272, doi:10.1029/JB093iB09p10255.

Smith, P. M., and P. D. Asimow (2005), Adiabat_1ph: A new public front-end to the MELTS, pMELTS, and pHMELTS models, *Geochem. Geophys. Geosyst.*, *6*, Q02004, doi:10.1029/2004GC000816.

Sohn, R. A., and K. W. W. Sims (2005), Bending as a mechanism for triggering off-axis volcanism on the East Pacific Rise, *Geology*, *33*(2), 93–96, doi:10.1130/G21116.1.

Sparks, D. W., and E. M. Parmentier (1991), Melt extraction from the mantle beneath spreading centers, *Earth Planet. Sci. Lett.*, *105*, 368–377, doi:10.1016/0012-821X(91)90178-K.

Spiegelman, M. (1993a), Flow in deformable porous media. Part 1. Simple analysis, *J. Fluid Mech.*, *247*, 17–38, doi:10.1017/S0022112093000369.

Spiegelman, M. (1993b), Flow in deformable porous media. Part 2. Numerical analysis—The relationship between shock waves and solitary waves, *J. Fluid Mech.*, *247*, 39–63, doi:10.1017/S0022112093000370.

Spiegelman, M. (1993c), Physics of melt extraction: Theory, implications and applications, *Phil. Trans. R. Soc. London*, *342*(1663), 23–41.

Spiegelman, M., and T. Elliott (1993), Consequences of melt transport for uranium series disequilibrium in young lavas, *Earth Planet. Sci. Lett.*, *118*, 1–20, doi:10.1016/0012-821X(93)90155-3.

Spiegelman, M., and D. McKenzie (1987), Simple 2-D models for melt extraction at MORs and island arcs, *Earth Planet. Sci. Lett.*, *83*, 137–152, doi:10.1016/0012-821X(87)90057-4.

Standish, J. J., and K. W. W. Sims (2010), Young off-axis volcanism along the ultraslow-spreading Southwest Indian Ridge, *Nat. Geosci.*, *3*, 286–292, doi:10.1038/ngeo824.

Standish, J. J., H. J. B. Dick, P. J. Michael, W. G. Melson, and T. O'Hearn (2008), MORB generation beneath the ultraslow spreading Southwest Indian Ridge (9–25E): Major element chemistry and the importance of process versus source, *Geochem. Geophys. Geosyst.*, *9*, Q05004, doi:10.1029/2008GC001959.

The MELT Seismic Team (1998), Imaging the deep seismic structure beneath a MOR: The MELT experiment, *Science*, *280*, 1215–1218, doi:10.1126/science.280.5367.1215.

Villiger, S., O. Müntener, and P. Ulmer (2007), Crystallization pressures of mid-ocean ridge basalts derived from major element variations of glasses from equilibrium and fractional crystallization experiments, *J. Geophys. Res.*, *112*, B01202, doi:10.1029/2006JB004342.

Warren, J. M., and N. Shimizu (2010), Cryptic variations in abyssal peridotite compositions: Evidence for shallow-level melt infiltration in the oceanic lithosphere, *J. Petrol.*, *51*, 395–423, doi:10.1093/petrology/egp096.

Warren, J. M., N. Shimizu, C. Sakaguchi, H. J. B. Dick, and E. Nakamura (2009), An assessment of upper mantle heterogeneity based on abyssal peridotite isotopic compositions, *J. Geophys. Res.*, *114*, B12203, doi:10.1029/2008JB006186.

White, R. S., T. A. Minshull, M. J. Bickle, and C. J. Robinson (2001), Melt generation at very slow-spreading oceanic ridges: Constraints from geochemical and geophysical data, *J. Petrol.*, *42*(6), 1171–1196, doi:10.1093/petrology/42.6.1171.

Wilson, D. S. (1993), Confidence intervals for motion and deformation of the Juan de Fuca plate, *J. Geophys. Res.*, *98*, 16,053–16,071, doi:10.1029/93JB01227.

Workman, R. K., and S. R. Hart (2005), Major and trace element composition of the depleted MORB mantle (DMM), *Earth Planet. Sci. Lett.*, *231*, 53–72, doi:10.1016/j.epsl.2004.12.005.

Yang, H. J., R. J. Kinzler, and T. L. Grove (1996), Experiments and models of anhydrous, basaltic olivine-plagioclase-augite saturated melts from 0.001 to 10 kbar, *Contrib. Mineral. Petrol.*, *124*, 1–18, doi:10.1007/s004100050169.

Yoder, H. S. (1965), Diopside-anorthite-water at five and ten kilobars and its bearing on explosive volcanism, *Year Book Carnegie Inst. Washington*, *64*, 82–89.